RSC Advances

ROYAL SOCIETY OF CHEMISTRY

www.rsc.org/advances

Controlled, template-free, and hydrothermal synthesis route to sphere-like α-Fe_2O_3 nanostructures for textile dye removal

Mostafa Y. Nassar*, Ibrahim S. Ahmed, Talaat Y. Mohamed, Mai Khatab

Chemistry Department, Faculty of Science, Benha University, Benha 13518, Egypt

*Corresponding authors. Tel.: +20 1068727555, Fax.: +20 133222578. E-mail addresses: m_y_nassar@yahoo.com, m_y_nassar@fsc.bu.eg.edu.

Abstract

Iron carbonate nanospheres were synthesized via hydrothermal treatment of aqueous solutions of iron sulfate, ascorbic acid and ammonium carbonate with a molar ratio of 1:1:3, respectively, at 140 ºC for 1.5 h. Pure α-Fe_2O_3 nanoparticles with an average crystallite size of 10.5-32 nm were produced by thermal decomposition of $FeCO_3$ at 400- 600 ºC for 2h. The compositions of the products were identified by means of XRD, FE-SEM, HR-TEM, FT-IR, BET, zeta potential and thermal analysis. The adsorption properties of α-Fe_2O_3 were evaluated using reactive red (RR) dye. Various parameters influencing the adsorption process were investigated, using a batch technique. The results exhibit that α-Fe_2O_3 nanoparticles show good adsorption capacity and the percent removal reaches about 98.77% in 10 min and increasing the surface area of the α-Fe_2O_3 nanoparticles from 107.7 to 165.6 m^2/g increases the adsorption capacity from 4.7 to 20.5 mg/g. Moreover, the adsorption data fit well the Langmuir isotherm model and the thermodynamic parameters exhibited an endothermic and spontaneous nature of the adsorption of RR dye on the hematite adsorbent.

Keywords: Hydrothermal synthesis; $FeCO_3$; Fe_2O_3 nanoparticles; Textile dye, Adsorption; Kinetics.

1.Introduction

Over the past few years, water pollution has been considered as one of the major threats to our world because it results in imbalance and significant alterations in the hydrological cycle which in turn cause many health problems and may even lead to death [1]. Synthetic organic dyes mainly produced from different industries (such as leather, paper, textile, plastic, refineries, and chemical) are mostly toxic, carcinogenic, and stable against photodegradation and these dyes along with heavy metals induce water pollution [2,3]. Hence, the wastewater generated from various industries has to be treated using an appropriate method before discharge, in order to get rid of these problems. There are several physical and chemical methods have been proposed for organic dye removal from wastewaters such as photodegradation, precipitation, filtration, coagulation, ion exchange, reverse osmosis, adsorption, etc. [4-8]. Among all the proposed attempts for dye removal, adsorption is still considered the most appropriate method in this concern due to its simplicity, economic applicability, high efficiency, and nonexistence of harmful species. Due to the high surface area of the nanomaterials, several research groups have focused their efforts on synthesizing of nanosized oxides using different routes and proposing them as good adsorbents [2-14].

On the other hand, nanosized iron oxides have recently received a considerable interest of several research groups as efficient adsorbents for the decontamination purpose of wastewater [8,15,16]. Among nano-sized iron (III) oxides, hematite, α-Fe_2O_3, is the most important and thermodynamically stable form under ambient conditions [17]. Due to its stability, non-toxicity, high efficiency, and inexpensive nature, hematite has been used in different applications such as

gas sensors, pigments, electrode materials, catalysts, magnetic resonance imaging, clinical therapy, magnetic materials, printing inks, ferrofluids, and water treatment [18-23]. These interesting properties and applications stimulated many material and inorganic researchers and hence to direct their efforts to synthesize α-Fe_2O_3 with different morphologies and particle sizes [24-27]. As a consequence, several methods such as micro-emulsion, sol-gel, hydro/solvothermal, microwave-assisted solvothermal, ultrasonic precipitation, mechanochemical, thermal decomposition, and sono-electrochemical anodization have been developed for the synthesis of nanosized α-Fe_2O_3 structures [27-34]. Although the methods that have been reported for synthesis of hematite are a lot, it is still a big challenge to have a facile and inexpensive methodology to control the morphology and particle size of the hematite nanostructures. So far, the hydrothermal technique still has the priority over the most synthetic methods due to its low-cost, simplicity, and varying morphologies of products [11]. Plus, there are different parameters; such as temperature, time, solvents, and precursors, for the hydrothermal process the researcher can tune them to control the purity, particle size, and morphology of the products. However, we have reported on the hydrothermal synthesis of $CoCO_3$ microspheres and their thermal conversion into cobalt oxide nanoparticles [5,11,12]. One of the most important aspects of producing of metal oxide nanoparticles through thermal conversion of metal carbonates is the formation of nano-pores due to the release of carbon dioxide from metal carbonate during the thermal decomposition step which results in novel nanostructures with relatively large specific surface area. Reports on similar synthetic routes for producing α-Fe_2O_3 via thermal decomposition of hydrothermally prepared ferrous carbonate are still limited [34-37]. In such, Liu et al. reported on synthesis of $FeCO_3$ microspheres using a surfactant-assisted hydrothermal reaction of iron chloride and urea [34]. Plus, Xaun et al. prepared $FeCO_3$ with still large particle size through the hydrothermal reaction of the same iron

salt with different carbonate source ($NaCO_3$) [35]. Also, Yang et al. reported on preparation of $FeCO_3$ microspheres using the relatively inexpensive iron sulfate salt via its hydrothermal treatment with urea but they used relatively large quantity of ascorbic acid in their procedure and their $FeCO_3$ have large particle size [36]. However, an extensive study on the hydrothermal treatment of $FeSO_4$ and $(NH_4)CO_3$ to produce $FeCO_3$ with smaller particle size using smaller quantity of ascorbic acid at relatively low temperature has not been reported so far.

In the current work, as a continuation to our previous study [5,11,12], a facile hydrothermal synthesis was adopted, for the first time, to synthesize spherical $FeCO_3$ nanoparticles in high yield by the reaction of iron sulfate and ammonium carbonate, as an inexpensive carbonate source, in presence of ascorbic acid. Different conditions affecting the synthesis process such as reaction temperature, molar ratio of the reactants, and reaction time have been investigated. Pure α-Fe_2O_3 nanoparticles are easily produced by thermal conversion of the as-prepared $FeCO_3$ in air. The as-prepared materials have been characterized by means of thermal analysis and different spectroscopic tools. The applicability of the as-prepared hematite nanoparticles was investigated for the removal of Reactive Red Me 4BL dye (RR) as a model pollutant from aqueous phase.

2.Experimental

2.1. Chemicals and Reagents

Unless otherwise stated, all chemicals and reagents in this work were of analytical grade and they were purchased and utilized as received without further purification: Iron sulfate ($FeSO_4.7H_2O$; Sigma-Alrich), ascorbic acid ($C_6H_8O_6$; Sigma-Alrich), and ammonium carbonate ($(NH_4)_2CO_3$; Fluka), Reactive Red Me 4BL dye (RR) ($C_{31}H_{19}ClN_7O_{19}S_6Na_5$; Rushabh chemicals industries, India).

2.2. Preparation of $FeCO_3$ and α-Fe_2O_3 nanoparticles

In a typical preparation procedure: Iron sulfate (1.95 g 7.0 mmol, 1 eq.) and ascorbic acid (1.23 g, 7 mmol,1 eq.) were dissolved in 45 mL distilled water under stirring. To the stirring solution, an aqueous ammonium carbonate solution (2.016 g, 21 mmol, 3 eq.) (25 mL) was added and the stirring was continued for 10 min. Afterwards, the produced reaction mixture was then transferred into a 100-mL Teflon-lined autoclave which in turn was placed in an electric oven maintained at 140 °C for 1.5 h. The autoclave was naturally cooled and the precipitate ($FeCO_3$) was centrifuged and washed several times with distilled water and ethanol and dried in an oven at ca. 60 °C overnight. However, in order to obtain the previously mentioned optimum conditions, different experimental parameters affecting this hydrothermal reaction such as temperature (120-160 ºC), time (0.5-3 h), and molar ratio (iron sulfate : ascorbic acid : ammonium carbonate; 1:-:6, 1:0.5:6, 1:1:6, 1:2:6, 1:3:6, 1:1:1, 1:1:2, 1:1:3, and 1:1:6) have been investigated.

The nanosized iron(II) carbonate product prepared at the optimized conditions of the hydrothermal process was calcined at 400, 500, or 600 °C for 2 h in air to produce α-Fe_2O_3 nanoparticles - with different crystallite sizes - denoted as Fe_2O_3-400, Fe_2O_3-500, and Fe_2O_3-600, respectively.

2.3. Characterization

The crystallinity and phase purity of the as-prepared products were identified via powder X-ray diffraction (XRD) by using 18 kW diffractometer (Bruker; model D8 Advance) with monochromated Cu-Kα radiation (l) 1.54178 A˚). Using a field emission scanning electron microscope (FE-SEM) connected with a microscope (JEOL JSM-6500F), FE-SEM images were taken. The high resolution transmission electron microscope (HR-TEM) images were obtained on a transmission electron microscope (JEM-2100) at an accelerating voltage of 200 kV by

dispersing the samples in ethanol ultrasonically on a copper grid. FT-IR spectra were recorded on FT-IR spectrometer (Thermo Scientific; model Nicolet iS10) from 4000 to 400 cm^{-1}. The UV-Vis spectra of adsorption studies were recorded using a Jasco UV-Vis spectrophotometer (Jasco; model v670). The thermal analysis measurements of the as-prepared iron carbonate were carried out on a thermal analyzer instrument (Shimadzu; model TA-60WS) in a nitrogen atmosphere with a heating rate of 15 ºC/min. BET (Brunauer-Emmet-Teller) surface area of the as-synthesized Fe_2O_3 products was performed on Quantachrome (Nova 2000 series, USA) using nitrogen adsorption-desorption measurements. The zeta potential of the nanosized hematite product was measured using a Zeta sizer nano series meter (Nano ZS, Malvern, UK).

2.4. Adsorption experiments

The adsorption experiments were carried out in a batch method performed under a continuous magnetic stirring using Reactive Red Me 4BL dye (RR) as an adsorbate model, Table 1. The RR dye is a commercial product and it is used as received from Rushabh chemicals industries company, India, without further purification. Different experimental factors affecting the adsorption process such as dye solution pH (1-9), contact time (5-70 min), temperature (25-45 ºC), initial concentration (10-50 ppm) and salt effect, have been investigated. In a typical batch experiment, 50 mL of an aqueous RR dye solution of a desired concentration was prepared by suitable dilution of a stock solution and by using 0.1 mol/L HCl or NaOH aqueous solutions the pH of the solution was adjusted. Afterwards, a known quantity (0.1 g) of dry α-Fe_2O_3 nanoparticles was added and the produced suspension in the conical flask was then allowed to magnetically stir (400 rpm) for a definite time at room temperature. According to the experimental conditions under investigation, the temperatures and concentrations of the adsorbate were varied. After a predetermined time of stirring, an aliquot was taken out of the

flask and the adsorbent was separated by centrifugation at 4000 rpm for about 4 min and then the concentration of the remaining dye in the supernatant solution was determined using UV-Vis spectrophotometer. It is noteworthy that analysis of the remaining dye concentration in the supernatant was carried out using a previously constructed calibration graph. The obtained data were used to calculate the adsorption capacities (q_t, mg/g) and the dye removal efficiencies (% Removal) using equations (1) and (2).

$$q_t = \frac{V(C_0 - C_t)}{m} \quad (1)$$

$$\% \text{ Removal} = \frac{(C_0 - C_t)}{C_0} \text{ x } 100 \quad (2)$$

where C_0 and C_t are the RR dye concentrations in mg/L at time =0 and t respectively in solution, V is the volume of dye solution (L), and m is the mass of dry α-Fe_2O_3 adsorbent (g).

3.Results and discussion

3.1. Hydrothermal synthesis and characterization of $FeCO_3$ nanospheres

Hydrothermal reactions of iron sulfate and ammonium carbonate in presence of ascorbic acid have been investigated in order to prepare pure iron carbonate. Fig.1(a) exhibits the XRD pattern of $FeCO_3$ nanospheres synthesized by the hydrothermal treatment of aqueous solutions of iron sulfate, ammonium carbonate and ascorbic acid at the optimal conditions: Fe^{2+}:ascorbic acid:CO_3^{2-} molar ratio of 1:1:3, 1.5 h reaction time, and 140 ºC reaction temperature. All the diffraction peaks can be indexed well to a pure rhombohedral phase of $FeCO_3$ which is in consistent with the standard patterns of iron carbonate (space group R-3c, JCPDS card 83-1764) [37]. No other characteristic peaks corresponding to iron oxides or even other impurities have been observed. The average crystallite size (D) of the as-prepared $FeCO_3$ was found to be 22 nm which was calculated using the Debye–Scherrer formula [38]:

$$D=0.9\lambda/\beta\cos\theta_B$$

where λ is the X-ray wavelength, β is the full width at half maximum (FWHM) of the diffraction peak and θ_B is the Bragg diffraction angle. The producing of the α-Fe_2O_3 nanoparticles, Fig.1(b), was performed through thermal conversion of the hydrothermally as-synthesized iron carbonate precursor at the optimal condition as will be explained later.

3.1.1. Optimization of the hydrothermal preparation of $FeCO_3$ nanoparticles

The optimum conditions for preparation of the pure iron carbonate have been reached by studying the various reaction conditions influencing the hydrothermal process such as reaction temperature, reaction time and iron sulfate:ascorbic acid:ammonium carbonate molar ratios using the XRD analysis.

3.1.1.1. Effect of temperature

Effect of temperature on the hydrothermal treatment of the reactants has been investigated first and Fig.2I(a-c) exhibits the XRD patterns of the hydrothermally produced products using molar ratio of 1:3:6 for iron sulfate:ascorbic acid:ammonium carbonate, respectively, for 3 h at different temperatures (160, 140, and 120 ºC). It can be noticed that the three temperatures produced iron carbonates and the optimum temperature was 140 ºC since it gave pure iron carbonate with a moderate crystallite size (80 nm). However, 160 ºC temperature gave pure product with very large crystallite size (200 nm), and 120 ºC produced the product with very poor crystallinity contaminated with some impurities as indicated from their XRD patterns and appearance of some peaks for some undefined by-products.

3.1.1.2. Effect of reaction time

Fig.2II(a-e) reveals the reaction time effect (3, 2, 1.5, 1, and 0.5 h) on the hydrothermal treatment of interest at 140 ºC with iron sulfate:ascorbic acid:ammonium carbonate molar ratio of 1:3:6. The results indicated that the optimum reaction time was 1.5 h. On the other hand, shorter time (i.e. <1.5 h) produced iron carbonate with poor crystallinity and low yield, and

longer time gave particles with very large crystallite size. On comparing the optimum temperature and time in the current study with other reported ones for preparing pure iron carbonate, it can easily be seen that we have used lower temperature and shorted time than the reported ones [34-36].

3.1.1.3. Effect of ascorbic acid concentration

Ascorbic acid in this study plays a remarkable role since it acts as a reducing agent preventing iron (II) ions from oxidation and its influence on the reaction has been studied. Fist this hydrothermal treatment has been carried out at 1.5 h reaction time, 140 ºC reaction temperature, a fixed Fe^{2+}:CO_3^{2-} molar ratio of 1:6 in absence of ascorbic acid, and the XRD pattern of the product is shown in Fig. 2III(a). Also, the influence of addition of different quantities of ascorbic acid have been explored by trying different Fe^{2+}:ascorbic acid:CO_3^{2-} molar ratios: 1:**0.5**:6, 1:**1**:6, 1:**2**:6, and 1:**3**:6; and the XRD results are depicted in Fig. 2III(b-e), respectively. Inspection of XRD patterns of the produced products (Fig. 2III) reveals that the minimum required equivalents of ascorbic acid is 1 (i.e. Fe^{2+}:ascorbic acid:CO_3^{2-} optimum molar ratio is 1:**1**:6) and using less equivalents of the ascorbic acid (i.e. < 1 equivalent) gives iron carbonate with poor crystallinity along with some impurities such as magnetite. It is worthy to mention that in the current hydrothermal treatment smaller quantity of ascorbic acid has been used to produce pure iron carbonate with smaller particle size on comparing to the other reported methods [34-36]. However, the mechanism of the current hydrothermal process can be explained according to the proposed Scheme 1 as follows: ammonium carbonate and iron sulfate generate carbonate and iron ions according to reactions i and ii, respectively. At the optimum or higher concentrations of both carbonate ions and ascorbic acid, the reactions iii and vii (Scheme 1) will be the more predominant reactions and accordingly the product will be pure iron carbonate. At lower concentration of ascorbic acid, Fe^{3+} ions (which result from oxidation of Fe^{2+} during

mixing or heating) will not completely be reduced to Fe^{2+} ions (reaction iv) and in turn Fe^{3+} ions will react with OH^- (which can be generated from reaction v) to produce $Fe(OH)_3$. Thence, there will be a competition between reactions iii, vii and ix and the result of that competition will be a mixture of iron carbonate and Fe_3O_4. Additionally, Fe_3O_4 impurities are by-products generated from the reaction between $Fe(OH)_3$ (reaction viii) and $Fe(OH)_2$ (reaction vi) at the hydrothermal conditions according to reaction ix (Scheme 1) and this is in agreement with the reported data [36].

3.1.1.4. Effect of Fe^{2+}:CO_3^{2-} molar ratios

Effect of ammonium carbonate concentration has been investigated by keeping Fe^{2+} ion and ascorbic acid concentrations constant and varying the concentration of ammonium carbonate by using the following different molar ratios:1:1:**1**, 1:1:**2**, 1:1:**3**, and 1:1:**6** for Fe^{2+}:ascorbic acid:CO_3^{2-}, respectively, and the XRD patterns of the products are given in Fig.2IV(a-d), respectively. The obtained results reveal that using lower concentration of CO_3^{2-} anion than 3 equivalents it will produce by-products along with $FeCO_3$ with very poor crystallinity. Consequently, it can be concluded that the optimum molar ratio for this template-free hydrothermal reaction is (1:1:3) for Fe^{2+}:ascorbic acid:CO_3^{2-}, respectively.

3.1.2. Morphological study

Fig.3(I) presents the FE-SEM images of the as-synthesized $FeCO_3$ nanostructures prepared under the optimized conditions with a low and high magnifications, respectively. It is obvious from the low magnification image, Fig. 2(I), that the iron carbonate product is almost composed of agglomerates of nanospheres and from the high magnification image, Fig. 2(Ib), average size of the nanospheres was estimated to be about 70 nm in the diameter. It is noticeably that pure iron carbonate with smaller particle size (70 nm) has been successfully synthesized hydrothermally on comparing to the previously reported results [34-36].

3.1.3. FT-IR study

Fig. 4(a) displays the IR spectrum of the as-synthesized $FeCO_3$ product and it reveals vibrational absorptions at 1392, 1109, 859, and 735 cm^{-1} attributing to the absorbance of pure iron carbonate product and these stretching vibrations are fingerprint of D_3h symmetry which in turn is an evidence for the presence of carbonate anions in the iron carbonate products [5,11,12,39]. The weak band appeared at 2457 cm^{-1} may be assigned to the stretching vibration of the carbonate anions [5,11,12,40]. Plus, the vibrational shoulder observed at 1780 cm^{-1} may be ascribed to the overtone or combination of some vibrational frequencies of divalent metal cations and the carbonate group bond [5,11,12,40]. The broad vibrational band at 3140 cm^{-1} and the band at 1660 cm^{-1} may be assigned to the stretching and the bending vibrations, respectively, of adsorbed water molecules interacting with CO_3^{2-} anions of the iron carbonate molecules [5,11,12,34].

3.1.4. Thermal study

The thermal conversion of the as-synthesized iron carbonate product investigated using TG analysis, Fig.5. Fig. 5 indicates the presence of 36.20% overall weight loss in two weight loss steps in the TG curve in the temperature ranges 25-100 ºC and 120-350 ºC. The first weight loss, ca. 3.0% (theoretical value, 3.75%), may be assigned to the loss of adsorbed/trapped water molecules from the iron carbonate sample, whereas the second step, 33.20% (theoretical value, 33.66%) may be due to the thermal conversion of $FeCO_3$ into Fe_2O_3, CO, and CO_2 under N_2 gas atmosphere, and this thermal behavior is similar to the that reported for $CoCO_3$ elsewhere [5,11,12].

3.2. Preparation and characterization of α-Fe_2O_3 nanoparticles

Based on the aforementioned thermal data, the as-synthesized iron carbonate nanospheres, prepared at the optimized conditions, were thermally heated up at 400 ºC for 2 h to produce pure

α-Fe_2O_3 nanoparticles. Fig.1(b) exhibits the XRD pattern of the iron oxide product and this pattern can be readily indexed to pure α-Fe_2O_3 phase with the hexagonal structure (space group R-3c, lattice constant; a= 5.038 Å and c=13.776 Å, JCPDS card 89-0598). The estimated average crystallite size of the produced α-Fe_2O_3 nanoparticles using the Debye-Scherrer equation [38] was found to be ca. 10.5 nm. Moreover, the as-prepared $FeCO_3$ precursor was also calcinated at 500 and 600 ºC to α-Fe_2O_3 nanoparticles with different crystallite size; 19.8 and 31.2 nm, respectively, calculated from the XRD patterns of the produced α-Fe_2O_3, Fig. 1(c,d), using the Debye-Scherrer equation. It is noticeable that higher calcination temperatures produced larger crystallite sizes. The surface morphology and microstructure of α-Fe_2O_3 particles produced at 600 ºC and displayed in Fig. 3(II) and Fig. 6 have been investigated using FE-SEM and TEM, respectively. It can be seen from Fig. 3(II) that α-Fe_2O_3 product is clusters of individually spherical shape α-Fe_2O_3 particles and this indicates that iron carbonate morphologies on calcination have almost been retained for α-Fe_2O_3 product. Inspection the size and morphology of the α-Fe_2O_3 particles, Fig.6, using TEM images exhibits that the α-Fe_2O_3 product consists of irregular and spherical morphology with an average particle size of ca. 32 nm which is consistent with the one obtained using XRD data. Chemical structure of α-Fe_2O_3 produced at 600 ºC (Fe_2O_3-600 product) was also confirmed by using Fourier transform infrared spectrum, Fig.4(b), which exhibited two strong absorption bands at 547.7 and 461.9 cm^{-1} corresponding to the Fe-O bond which is consistent with the published data [21,41,42]. Plus, the two bands appeared at 3370 and 1600 cm^{-1} can be attributed to the stretching and bending vibrations of adsorbed surface water molecules interacting with the oxide product and the broadness of these peaks may be assigned to hydrogen bonding O-H [39].

3.2.1. Point of zero charge (PZC) and isoelectric point (IEP)

The point of zero charge (pH_{pzc}) of Fe_2O_3 nanoparticles calcinated at 600 ºC (Fe_2O_3-600) was estimated by the pH drift method as reported by Ahmaruzzaman et al [43]. It is notably, pH_{pzc} is the pH at which charge on the Fe_2O_3 nanoparticles is zero. The pH_{pzc} of the Fe_2O_3 was determined as follows: 25 mLs of 0.01 M NaCl solution with initial pH ($pH_{initial}$) in the range between 2.0 and 10.0 adjusted with 0.1 M NaOH or 0.1 M HCl solution. Then, each NaCl solution (25 mL) was added to 0.05 g of the Fe_2O_3 adsorbent then left to stir for 48 h. The mixture was centrifuged and pH the supernatant was measured (pH_{final}). Fig. 7(a), exhibits the plotting of $pH_{initial}$ versus pH_{final} and the point at which the curve $pH_{initial}$ - pH_{final} intersects the $pH_{initial}$=pH_{final} is the pH_{pzc}. The pH_{pzc} value of the Fe_2O_3 adsorbent was estimated to be ca. 6.8 which is in agreement with the published data [44,45].

On the other hand, the pH of the isoelectric point (IEP) was determined by plotting the zeta potentials of Fe_2O_3 suspensions in 0.01 M NaCl solutions at various pH range from 2 to 10, as shown in Fig. 7(b). The pH was adjusted with 0.1 M NaOH or 0.1 M HCl solutions. The pH value of the isoelectric point (IEP) was found to be ca. 7.1 which is in consistent with the published data [44-46].

3.3. Adsorption properties of α-Fe_2O_3 nanoparticles

Adsorption properties of the α-Fe_2O_3 nanoparticles calcinated at 600 ºC (Fe_2O_3-600) were investigated by choosing RR dye as an adsorbate model.

3.3.1. Effect of pH

Initial pH of the solution plays an important role in the adsorption experiments because it influences the surface binding sites of the nanoparticles acting as adsorbents and the dye speciation, as well. Effect of the initial pH (1-9) of the solution on the adsorption of the RR dye (C_0=20 ppm, λ_{max}=542 nm) on α-Fe_2O_3 nanoparticles (m=0.1 g) for 24 h as contact time was

investigated and presented in Fig. 8. The data exhibited that the adsorption was pH dependent and the maximum adsorption was observed to be in the range of pH 1-3. Afterwards, the adsorption decreased slowly by increasing pH up to almost 5 then decreased significantly at higher pH values. Therefore, the other adsorption experiments in this study were carried out at pH 2, as an optimized pH value. This phenomenon may be explained on the basis that at pHs lower than pH_{pzc} or IEP (pH_{pzc}=6.8 and IEP=7.1 for α-Fe_2O_3 nanoparticles), the surface of the α-Fe_2O_3 is positively charged and hence the attraction between the oppositely charges (i.e. these positively charges and the negatively charged RR dye) results in higher adsorption. Consequently, at pHs higher than pH_{pzc} or IEP there will be an electrostatic repulsion between the negatively charged α-Fe_2O_3 surface and the negatively charged RR dye and this may be the reason for lower adsorption at higher pH values.

3.3.2. Effect of initial dye concentration

The dependence of the adsorption of RR dye on the RR dye initial concentration (10-50 ppm) was investigated at room temperature and pH 2 and presented in Fig. 9. It can be clearly observe that the removal efficiency decreases from 95.5% to 42.6% with increasing the dye initial concentration from 10 ppm to 50 ppm, respectively. This may be attributed to saturation of the adsorption surface sites on the α-Fe_2O_3 adsorbent on increasing the dye initial concentration.

3.3.3. Effect of ionic strength

The presence of dissolved inorganic ions is well known problem in wastewater containing industrial dyes [47]. These dissolved ions can compete with the dye of interest for the adsorption on the active sites on the adsorbent surface and hence this may reduce the adsorption efficiency of the dyes. In this study, influence of ionic strength by addition of KCl salt to the dye solution (30 ppm) on the adsorption process was investigated and presented in Fig. 10. The data

indicate the decrease of the dye removal by increasing the KCl concentration because ions of the salt compete with the RR dye in adsorption by α-Fe_2O_3 adsorbent.

3.3.4. Effect of contact time on the adsorption and the kinetic studies

The effect of contact time on the adsorption of RR dye was investigated at the optimized pH 2, 0.1 g adsorbent, and 10 ppm dye initial concentration, as shown in Fig.11. It can be seen that the adsorption amount increased rapidly and reached about 95.5% in only 10 min and afterwards it stayed almost constant. Hence, 10 min was selected as the optimized contact time for the remaining study. This rapid adsorption may be attributed to the presence of large number of surface sites for the α-Fe_2O_3 nanoparticles available for adsorption.

To gain some information about the adsorbate amount and the rate of the adsorption process, kinetic parameters of RR dye adsorption on the α-Fe_2O_3 adsorbent were calculated by applying pseudo-first order equation [48], pseudo-second order equation [49], and intraparticle diffusion model [50], as shown in Fig 12(a-c), respectively. It is noteworthy that the validity and fitting of the kinetic model can be examined by checking the value of the linear regression which is also known as a correlation coefficient, r. The linear form of pseudo-first order kinetic model is:

$$\log(q_e - q_t) = \log q_e - \frac{k_1}{2.303} t \qquad (3)$$

where k_1 (min^{-1}) is the pseudo-first order rate adsorption constant, q_e (mg/g) is the adsorption capacity at equilibrium, and q_t (mg/g) is the adsorption capacity at time t (min). Plus, values of k_1 can be determined from plotting of $\log(q_e - q_t)$ against t, Fig 12(a). However, the obtained experimental data did not fit the pseudo-first order kinetic model, and the straight line could not be obtained, hence we tried to fit the adsorption data using pseudo-second order kinetic model. The linear form of the pseudo-second order kinetic equation can be given as follows:

$$\frac{t}{q_t} = \frac{1}{k_2\, q_e^2} + \frac{t}{q_e} \qquad (4)$$

Where k_2 ((g/mg).min) is the rate constant of pseudo-second order rate adsorption constant which can be calculated from plotting of t/q_t against t as shown in Fig. 12(b). The adsorption kinetic constants including the calculated equilibrium adsorption capacity $q_{e(cal)}$ and the experimental equilibrium adsorption capacity $q_{e(exp)}$ for the adsorption of RR dye on α-Fe_2O_3 adsorbent are presented in Table 1. Based on Fig 12(a,b) and the values of the regression coefficients presented in Table 2, it is clearly obvious that the adsorption of RR dye on α-Fe_2O_3 adsorbent can be described well by pseudo-second order model. Plus, the experimental adsorption capacity value ($q_{e(exp)}$) is consistent with the calculated one ($q_{e(cal)}$). However, in order to gain further insight into the rate determining step involved in the adsorption of RR dye on α-Fe_2O_3 adsorbent, intra-particle diffusion model was examined by applying the Weber and Morris equation:

$$q_t = k_i t^{0.5} + C \qquad (5)$$

where k_i is the intra-particle diffusion constant (mg/(g $min^{1/2}$)), and C represents the boundary layer thickness (mg/g). According to this model, plotting of qt values against $t^{0.5}$ values should give a straight line which passes through the origin, if the rate determining step is the intra-particle diffusion. Otherwise, boundary layer diffusion or chemical reaction is the rate determining step. In the current case, the obtained plot (Fig. 12(c)) is a multilinear and not passing the origin which indicates that the overall adsorption process may be proceed by more than one mechanism such as film diffusion, chemical reaction, and intra-particle diffusion [51].

3.3.5. Adsorption isotherms

Adsorption results have been analyzed using the two well-known isotherms; Langmuir and Freundlich models. These two models can be applied to describe the adsorption capacity of

the adsorbent at different equilibrium concentrations of the dye at the optimized adsorption conditions. The linear form of the Langmuir relationship can be expressed as follows:

$$\frac{C_e}{q_e} = \frac{1}{K_L q_m} + \frac{C_e}{q_m} \qquad (6)$$

where C_e is the equilibrium concentration of the RR dye in solution (mg/L), q_e is the equilibrium adsorption capacity of the RR dye on the α-Fe_2O_3 adsorbent, q_{max} is the maximum of adsorbed solute to form a monolayer per gram of adsorbent (mg/g), and K_L is the Langmuir adsorption constant (L/mg). The constants K_L and q_{max} can be calculated from the slope and intercept of the linear plot of C_e/q_e versus C_e (Fig.13(a)). The linear form of the Freundlich isotherm can be given as follows:

$$\ln q_e = \ln K_F + \frac{1}{n} \ln C_e \qquad (7)$$

where n and K_F are Freundlich constants related to adsorption intensity and adsorption capacity of the α-Fe_2O_3 adsorbent, respectively, and they are obtained from the slope and intercept of the linear plot of $\ln q_e$ against $\ln C_e$ (Fig.13(b)). The Langmuir and Freundlich constants are presented in Table.3. Clearly, the adsorption of RR dye on the α-Fe_2O_3 adsorbent follows the Langmuir adsorption isotherm model and the correlation coefficient for this model is estimated to be 0.992. Plus, fitting of the experimental data to Langmuir isotherm model exhibits the homogeneous nature of α-Fe_2O_3 surface which in turn means that each RR dye molecule/adsorption has equal activation energy of adsorption. Hence, the results reveal that the adsorption of the RR dye is monolayer coverage at the outer surface of α-Fe_2O_3 adsorbent. Moreover, the efficiency of the adsorption of the RR dye on the adsorbent can be estimated through the values of the separation factor constant (R_L) which can be given as follows:

$$R_L = \frac{1}{1 + K_L C_o} \qquad (8)$$

where C_0, and K_L are the initial concentration (mg/L) and the Langmuir constant (L/mg), respectively. The value of the R_L indicates whether the isotherm type is irreversible $R_L=0$, favorable $0<R_L<1$, linear $R_L=1$, or unfavorable $R_L>1$. The calculated R_L value in the current case is found to be 0.00615 which refers to that the adsorption of the RR dye on the α-Fe_2O_3 adsorbent is favorable in this investigation at the optimized adsorption conditions.

3.3.6. Thermodynamic adsorption studies

Influence of the temperature on the adsorption process was investigated by studying the adsorption of RR dye on the α-Fe_2O_3 adsorbent at different temperature; 303, 313, and 323 K. It is found that the adsorption capacity increases from 11.36 to 12.18 mg/g on increasing temperature from 303 to 323 K. This is an indication that the adsorption of RR dye on α-Fe_2O_3 nanoparticles is an endothermic process. The thermodynamic parameters such as standard Gibbs free energy (ΔG^0), standard enthalpy (ΔH^0), and standard entropy (ΔS^0) can be estimated using the following equations [52]:

$$\ln K_c = \frac{\Delta S^0}{R} - \frac{\Delta H^0}{RT} \qquad (9)$$

$$\Delta G^0 = -RT\ln K_c \qquad (10)$$

$$\Delta G^0 = \Delta H^0 - T\Delta S^0 \qquad (11)$$

where K_c is the thermodynamic equilibrium constant (L/g) given by q_e/C_e, R is the universal gas constant (8.314 J/(mol K)), and T is the absolute solution temperature (K). As clear from equation 9, Plotting of $\ln K_c$ against 1/T gives a straight line (Fig.14), ΔS^0 and ΔH^0 are calculated from the slope and intercept, and presented in Table.4. Inspection of Table.4 reveals the endothermic nature of the adsorption process as indicated from the positive value of the ΔH^0. Plus, the negative value of the ΔG^0 means that the adsorption of RR dye on the hematite nanoparticles is a spontaneous nature and the decrease in ΔG^0 values with increasing the temperature indicates that the adsorption process is more preferable at higher temperatures.

3.3.7. Surface area influence on the adsorption process and Fe_2O_3 adsorbent reusability

One of the factors that can influence in the adsorption process is the surface area of the adsorbents. The BET surface area (using nitrogen adsorption–desorption isotherms), BJH pore size, total pore volume, and crystallite size (calculated from the Debye–Scherrer equation) of the nano-sized products (Fe_2O_3-400, Fe_2O_3-500, and Fe_2O_3-600) were investigated and the results are tabulated in Table 5. The results exhibited that the order of BET surface areas for Fe_2O_3 products was Fe_2O_3-400 > Fe_2O_3-500 > Fe_2O_3-600. Also, the BJH pore volumes for the Fe_2O_3 nanostructures were in the same order.

However, as expected, the crystallite size of the aforementioned Fe_2O_3 products was in the reverse order. Moreover, in order to investigate the influence of the specific surface areas of the iron oxide products on the adsorption process, adsorption capacities of the products toward the RR dye were determined under the previously obtained optimum conditions and presented in Table 5. It is clear from this Table that Fe_2O_3-400 adsorbent has the highest adsorption capacity (20.5 mg/g) and the order of the adsorption capacities of the iron oxide products is in the same order as that for the surface areas. This can be explained based on that the higher surface area provides more contact and exposed sites for dye adsorption and hence this results in higher adsorption capacity.

On the other hand, reusability (i.e. recycling) of the adsorbents for industrial applications purposes is a crucial factor for choosing the suitable adsorbents. Hence, studying the recycling of the Fe_2O_3-400 adsorbent was performed by regenerating the RR-loaded adsorbent using either stirring the iron oxide in methanol for 5 h, washing with methanol, and drying at 60 ºC for ca. 5 h; or by carrying out combustion of the loaded adsorbent at 500 ºC for 30 min. The adsorption of the dye at the optimum conditions and regeneration of the loaded adsorbent was repeated for five times and the percent RR dye removal efficiency for the five recycles was depicted in Fig. 14.

adsorption. The results indicate that even after five recycles, Fe_2O_3-400 adsorbent still has high adsorption efficiency (ca. 94% RR dye removal efficiency). The good reusability data suggest that the as-prepared iron oxide adsorbent is an efficient adsorbent and the data also support the long term use of the adsorbent in water treatment from RR dye.

4. Conclusion

In the present work, pure $FeCO_3$ nanospheres were successfully synthesized in high yield smaller particle size and different morphology on comparing to the literatures by hydrothermal reaction of iron sulfate, ascorbic acid as reducing agent, and ammonium carbonate at 140 ºC for 3 h with molar ratio of 1:3:6, respectively. Afterwards, α-Fe_2O_3 nanoparticles were produced by heating of the as-prepared iron carbonate at 400, 500, or 600 ºC for 2h. The as-prepared products were characterized by means of FE-SEM, XRD, FT-IR, HR-TEM, BET, zeta potential, and thermal analysis. The adsorption properties of the as-prepared hematite nanoparticles were investigated using reactive red (RR) dye and the results exhibited good adsorption capacity of the nanosized adsorbent. Plus, the α-Fe_2O_3 nanoparticles produced at 400 ºC have the highest adsoption capacity since they have the highest BET surface area. The adsorption data fitted very well with the Langmuir isotherm model indicating that the adsorption reaction was essentially monolayer. The spontaneous and endothermic natures of the adsorption process were confirmed form the thermodynamic studies.

Acknowledgement

The authors thank Benha University, Egypt, for providing the required financial support to perform this research work.

References

[1] S. Qadri, A. Ganoe, Y. Haik, Removal and recovery of acridine orange from solutions by use of magnetic nanoparticles, J. Hazard. Mater. 169 (1-3) (2009) 318-323.

[2] B. Tanhaei, A. Ayati, M. Lahtinen, M. Sillanpaa, Preparation and characterization of a novel chitosan/Al_2O_3/magnetite nanoparticles composite adsorbent for kinetic, thermodynamic and isotherm studies of methyl orange adsorption, Chem. Eng. J. 259 (2015) 1-10.

[3] F. Qin, G. Li, H. Xiao, Z. Lu, H. Sun, R. Chen, Large-scale synthesis of bismuth hollow nanospheres for highly efficient Cr(VI) removal, Dalton Trans. 41(2012) 11263-11266.

[4] M.Y. Nassar, I.S. Ahmed, A novel synthetic route for magnesium aluminate ($MgAl_2O_4$) nanoparticles using sol-gel auto combustion method and their photocatalytic properties, Spectrochim. Acta part A 131 (2014) 320-334.

[5] M.Y. Nassar, I.S. Ahmed, Template-free hydrothermal derived cobalt oxide nanopowders: Synthesis, characterization, and removal of organic dyes, Mater. Res. Bull. 47 (2012) 2638–2645.

[6] B. Bi, L. Xu, B. Xu, X. Liu, Heteropoly blue-intercalated layered double hydroxides for cationic dye removal from aqueous media, Applied Clay Science 54 (2011) 242-247.

[7] Maryam Khosravi, Saeid Azizian, Adsorption of anionic dyes from aqueous solution by iron oxide nanospheres, J. Ind. Eng. Chem. 20 (2014) 2561 – 2567.

[8] H. Guo, J. Chen, W. Weng, Z. Zheng, D. Wang, Adsorption behavior of Congo red from aqueous solution on La_2O_3-doped TiO_2 nanotubes, 20 (2014) 3081- 3088.

[9] M.Y. Nassar , T.Y. Mohamed, I.S. Ahmed, One-pot solvothermal synthesis of novel cobalt salicylaldimine-urea complexes: A new approach to Co_3O_4 nanoparticles, J. Mol. Struct. 1050 (2013) 81-87.

[10] M.Y. Nassar, A.S. Attia, K.A. Alfallous, M.F. El-Shahat, Synthesis of two novel dinuclear molybdenum(0) complexes of quinoxaline-2,3-dione: New precursors for preparation of α-MoO_3 nanoplates, Inorg. Chim. Acta 405 (2013) 362–367.

[11] M.Y. Nassar, Size-controlled synthesis of $CoCO_3$ and Co_3O_4 nanoparticles by free-surfactant hydrothermal method, Mater. Lett. 94 (2013) 112-115.

[12] M.Y. Nassar, I.S. Ahmed, Hydrothermal synthesis of cobalt carbonates using different counter ions: An efficient precursor to nano-sized cobalt oxide (Co_3O_4), Polyhedron 30 (2011) 2431-2437.

[13] T.G. Venkatesha, R. Viswanatha, Y.A. Nayaka, B.K. Chethana, Kinetics and thermodynamics of reactive and vat dyes adsorption on MgO nanoparticles, Chem. Eng. J. 198-199 (2012) 1-10.

[14] H. Emadi, A.N. Kharat, Synthesis and characterization of ultrafine and mesoporous structure of cobalt ferrite, J. Ind. Eng. Chem. 21(2015) 951-956.

[15] Z. Zhang, J. Kong, Novel magnetic Fe_3O_4@C nanoparticles as adsorbents for removal of organic dyes from aqueous solution, J. Hazard. Mater. 193 (2011) 325-329.

[16] H. Li, Z. Lu, G. Cheng, K. Rong, F. Chen, R. Chen, HEPES-involved hydrothermal synthesis of Fe_3O_4 nanoparticles and their biological application, RSC Adv. 5 (2015) 5059-5067.

[17] H. Li, Z. Lu, Q. Li, M.-H. So, C.-M. Che, R. Chen, Hydrothermal synthesis and properties of controlled α-Fe_2O_3 nanostructures in HEPES solution, Chem. Asian J. 6 (2011) 2320 - 2331.

[18] H. Liang, W. Chen, Y. Yao, Z. Wang, Y. Yang, Hydrothermal synthesis, self-assembly and electrochemical performance of α-Fe_2O_3 microspheres for lithium ion batteries, Ceram. Int. 40 (2014) 10283–10290.

[19] A.S. Teja, P.Y. Koh, Synthesis, properties, and applications of magnetic iron oxide nanoparticles, Prog. Cryst. Growth Charact. Mater. 55 (2009) 22-45.

[20] M. Khalil, J. Yu, N. Liu, R.L. Lee, Non-aqueous modification of synthesized hematite nanoparticles with oleic acid, Colloid. Surf. A: Physicochem. Eng. Aspects 453 (2014) 7-12.

[21] M. Mohammadikish, Hydrothermal synthesis, characterization and optical properties of ellipsoid shape α-Fe_2O_3 nanocrystals, Ceram. Int. (2013), http://dx.doi.org/10.1016/j.ceramint.2013.07.016.

[22] M.-C. Huang, The optical, structural and photoelectrochemical characteristics of porous hematite hollow spheres prepared by DC magnetron sputtering process via polystyrene spheres template, Ceram. Int. 40 (2014) 10537-10544.

[23] J. Xie, Z. Zhou, Y. Lian, Y. Hao, P Li, Y. Wei, Synthesis of α-Fe_2O_3/ZnO composites for photocatalytic degradation of pentachlorophenol under UV-vis light irradiation, Ceram. Int. 41 (2015) 2622-2625.

[24] M. Gotić, G. Dražić, S.Musić, Hydrothermal synthesis of α-Fe_2O_3 nanorings with the help of divalent metal cations, Mn^{2+}, Cu^{2+}, Zn^{2+} and Ni^{2+}, J. Mol. Struct. 993 (2011) 167-176.

[25] C. Wu, P. Yin, X. Zhu, C.O. Yang, Y. Xie, Synthesis of hematite (α-Fe_2O_3) nanorods: diameter-size and shape effects on their applications in magnetism, lithium ion battery, and gas sensors, J. Phys. Chem. B110 (2006) 17806-17812.

[26] S. Rahimi, R.M. Moattaria, L. Rajabia, A.A. Derakhshanb, M. Keyhani, Iron oxide/hydroxide (α,γ-FeOOH) nanoparticles as high potential adsorbents for lead removal from polluted aquatic media, J. Ind. Eng. Chem. 23 (2015) 33-43.

[27] H. Wu, G. Wu , L. Wang, Peculiar porous α-Fe_2O_3, γ-Fe_2O_3 and Fe_3O_4 nanospheres: Facile synthesis and electromagnetic properties, Powder Technology 269 (2015) 443-451.

[28] G. Wu, X. Tan, G. Li, C. Hu, Effect of preparation method on the physical and catalytic property of nanocrystalline Fe_2O_3, J. Alloys Compd. 504 (2010) 371-376.

[29] A.A. Ayachia, H. Mechakra, M.M. Silvan, S. Boudjaadar, S. Achour, Monodisperse α-Fe_2O_3 nanoplatelets: Synthesis and characterization, Ceram. Int. l41(2015) 2228-2233.

[30] T.-W. Sun, Y.-J. Zhu, C. Qi, G.-J. Ding, F. Chen, J. Wu, α-Fe_2O_3 nanosheet-assembled hierarchical hollow mesoporous microspheres: Microwave-assisted solvothermal synthesis and application in photocatalysis, J. Colloid Interface Sci. 463 (2016) 107-117.

[31] X.-L. Cheng, J.-S. Jiang, C.-Y. Jin, C.-C. Lin, Y. Zeng, Q.-H. Zhang, Cauliflower-like α-Fe_2O_3 microstructures: Toluene–water interface assisted synthesis, characterization, and applications in wastewater treatment and visible-light photocatalysis, Chem. Eng. J. 236 (2014) 139-148.

[32] S. Sivakumar, D. Anusuya, C.P. Khatiwada, J. Sivasubramanian, A. Venkatesan, P. Soundhirarajan, Characterizations of diverse mole of pure and Ni-doped α-Fe_2O_3 synthesized nanoparticles through chemical precipitation route, Spectrochim. Acta Part A 128 (2014) 69-75.

[33] D. Wang, M. Zhang, J. Yuan, Y. Lin, C. Song, Facile route to Ni-doped α-FeOOH and α-Fe_2O_3 nanostructures and their properties, Mater. Lett. (2015), http://dx.doi.org/10.1016/j.matlet.2015.05.022i.

[34] X.J. Liu, H. Wang, C.H. Su, P.W. Zhang, J.B. Bai, Controlled fabrication and characterization of microspherical $FeCO_3$ and α-Fe_2O_3, J. Colloid Interface Sci. 351(2010) 427-432.

[35] S. Xuan, M. Chen, L. Hao, W. Jiang, X. Gong, Y. Hu, Z. Chen, Preparation and characterization of microsized $FeCO_3$, Fe_3O_4 and Fe_2O_3 with ellipsoidal morphology, J. Magn. Magn. Mater. 320 (2008) 164–170.

[36] T. Yang, Z. Huang, Y. Liu, M. Fang, X. Ouyang, M. Hu, Controlled synthesis of porous $FeCO_3$ microspheres and the conversion to α-Fe_2O_3 with unconventional morphology, Ceram. Int. 40 (2014) 11975-11983.

[37] M. Chirita, A. Ieta, $FeCO_3$ microparticle synthesis by Fe-EDTA hydrothermal decomposition, Cryst. Growth Des. 12 (2012) 883-886.

[38] R. Jenkins, R.L. Snyder, Chemical Analysis: Introduction to X-ray Powder Diffractometry, New York: John Wiley and Sons, Inc.; 1996.

[39] K. Nakamoto, Infrared and Raman spectra of inorganic and coordination compounds; Pt. B: Applications in coordination, organometallic, and bioinorganic chemistry, 5th Edn. USA: Wiley-Interscience; 1997.

[40] K.T. Ehlsissen, A. Delahaya-Vidal, P. Genin, M. Figlarz, P. Willmann, Preparation and characterization of turbostratic Ni/Al layered double hydroxides for nickel hydroxide electrode applications, J. Mater. Chem. 3 (1993) 883-888.

[41] R. Suresh, K. Giribabu, R. Manigandan, A. Stephen, V. Narayanan, Fe_2O_3@polyaniline nanocomposite: Characterization and unusual sensing property, Mater. Lett. 128 (2014) 369-372.

[42] R.A. Bepari, P. Bharali, B.K. Das, Controlled synthesis of α and γ-Fe_2O_3 nanoparticles via thermolysis of PVA gels and studies on α-Fe_2O_3 catalyzed styrene epoxidation, J. Saud. Chem. Soc. (2014), http://dx.doi.org/10.1016/j.jscs.2013.12.010.

[43] M. Ahmaruzzaman, S.L. Gayatri, Batch adsorption of 4-nitrophenol by acid activated jute stick char: Equilibrium, kinetic and thermodynamic studies, Chem. Eng. J. 158 (2010) 173-180.

[44] M. Kosmulski, pH-dependent surface charging and points of zero charge II. Update, J. Colloid Interface Sci. 275 (2004) 214-224.

[45] M. Kosmulski, E. Maczka, E. Jartych, J.B. Rosenholm, Synthesis and characterization of goethite and goethite–hematite composite: experimental study and literature survey, Adv. Colloid Interfac. 103 (2003) 57-76.

[46] E. Liu, H. Zhao, H. Li, Guangfang Li, Y. Liu, R. Chen, Hydrothermal synthesis of porous α-Fe_2O_3 nanostructures for highly efficient Cr(VI) removal, New J. Chem. 38 (2014) 2911-2916.

[47] N.M. Mahmoodi, F. Najafi, Preparation of surface modified zinc oxide nanoparticle with high capacity dye removal ability, Mater. Res. Bull. 47 (2012) 1800-1809.

[48] M.N. Sepehr, V. Sivasankar, M. Zarrabi, M.S. Kumar, Surface modification of pumice enhancing its fluoride adsorption capacity: an insight into kinetic and thermodynamic studies, Chem. Eng. J. 228 (2013) 192-204.

[49] Y.S. Ho, G. McKay, Pseudo-second order model for sorption processes, Process Biochem. 34 (1999) 451-465.

[50] W.J. Weber Jr., J.C. Morris, Kinetics of adsorption on carbon from solution, J. Sanitary Division Eng., Proc. Amer. Soc. Civ. Eng. 89 (1963) 31-59.

[51] C. Luo, Z. Tian, B. Yang, L. Zhang, S. Yan, Manganese dioxide/iron oxide/acid oxidized multi-walled carbon nanotube magnetic nanocomposite for enhanced hexavalent chromium removal, Chem. Eng. J. 234 (2013) 256-265.

[52] J. Zhou, Z. Zhang, B. Cheng, J. Yu, Glycine-assisted hydrothermal synthesis and adsorption properties of crosslinked porous α-Fe_2O_3 nanomaterials for p-nitrophenol, Chem. Eng. J. 211-212 (2012) 153-160.

Table and Figure captions

Table 1. Characteristics and chemical structure of Reactive red Me 4BL dye.

Table 2. Kinetic constants for RR dye adsorption on α-Fe_2O_3 nanoparticles.

Table 3. Isotherm parameters for RR dye adsorption of on α-Fe_2O_3 nanoparticles.

Table 4. Thermodynamic parameters for RR dye adsorption on α-Fe_2O_3 nanoparticles.

Table 5. BET surface area, pore size, pore volume, and crystallite size of Fe_2O_3 products and its removal capacity for RR dye.

Scheme 1. Proposed reaction mechanism for formation of $FeCO_3$ or a mixture of $FeCO_3$ and Fe_3O_4.

Fig. 1. XRD patterns of the as-synthesized $FeCO_3$ (a), and α-Fe_2O_3 nanoparticles produced at: 400 ºC (b), 500 ºC (c), and 600 ºC (d).

Fig 2I(a-c). XRD patterns of the $FeCO_3$ samples prepared under hydrothermal conditions for 3 h with molar ratio of 1:3:6 for iron sulfate:ascorbic acid:ammo-nium carbonate, respectively, at different temperatures: 120 (a), 140 (b), and 160 ºC (c).

Fig.2II(a-e). XRD patterns of the samples prepared under hydrothermal conditions with molar ratio of 1:3:6 for iron sulfate:ascorbic acid:ammonium carbonate, respectively, at 140 ºC for 0.5 (a), 1 (b), 1.5 (c), 2 (d), and 3h (e).

Fig. 2III(a-e). XRD patterns of the samples prepared under hydrothermal conditions with Fe^{2+}:CO_3^{2-} molar ratios of 1:6 (a), and with Fe^{2+}:ascorbic acid:CO_3^{2-} molar ratios of 1:0.5:6 (b), 1:1:6 (c), 1:2:6 (d), and 1:3:6 (e), at 140 ºC for 1.5h.

Fig. 2IV(a-d). XRD patterns of the samples prepared under hydrothermal conditions with Fe^{2+}:ascorbic acid:CO_3^{2-} molar ratios of 1:1:**1** (a), 1:1:**2** (b), 1:1:**3** (c), and 1:1:**6** (d), at 140 ºC for 1.5h.

Table 1. Characteristics and chemical structure of Reactive red Me 4BL dye.

Dye name	Reactive red Me 4BL, RR4BL
Chemical Structure	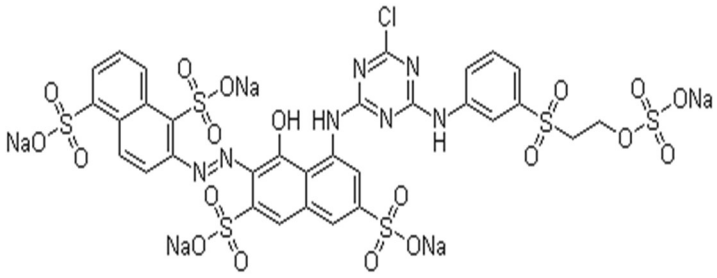
Molecular formula	$C_{31}H_{19}ClN_7O_{19}S_6Na_5$
Chemical class	Azo derivative compound
λ_{max}	542 nm
Type	Anionic dye
Solubility	Water soluble
C.I. number	Reactive Red 195

Table 2. Kinetic constants for RR dye adsorption on α-Fe_2O_3 nanoparticles.

Kinetics models	Parameters	Value
Pseudo-first order	K_1 (min^{-1})	0.036
	$q_{e(cal)}$ (mg/g)	4.70
	r_1^2	0.339
	$q_{e(exp)}$ (mg/g)	0.042
Pseudo-second order	K_2 [g/(mg min)]	0.208
	$q_{e(cal)}$) (mg/g)	4.70
	r_2^2	0.999
	$q_{e,exp}$ (mg/g)	4.81

Table 3. Isotherm parameters for RR dye adsorption of on α-Fe_2O_3 nanoparticles.

isotherm models	constants	Value
Langmuir	K_L (L/mg)	3.23
	$q_{m(cal)}$ (mg/g)	4.87
	r_1^2	0.992
	R_L	0.0062
	$q_{e(exp)}$ (mg/g)	4.70
Freundlich	K_F (mg/g)$(L/mg)^{1/n}$	6.65
	$q_{e(cal)}$) (mg/g)	20.7
	r_2^2	0.844
	n	4.02
	$q_{e,exp}$ (mg/g)	4.70

Table 4. Thermodynamic parameters for RR dye adsorption on α-Fe_2O_3 nanoparticles.

Temperature (K)	$\ln K_c$	ΔG^0 (kJ/mol)	ΔH^0 (kJ/mol)	ΔS^0 (kJ/mol K)
303	10.20	-18.509		
313	10.43	-19.851	13.587	0.106
323	10.45	-20.609		

Table 5. BET surface area, pore size, pore volume, and crystallite size of Fe_2O_3 products and its removal capacity for RR dye.

Adsorbent sample	BET surface area, m^2/g	Crystallite size, nm	BJH pore diameter (nm)	BJH Pore volume (cm^3/g)	Removal adsorption capacity (mg/g)
Fe_2O_3-400	165.6	10.5	2.24	0.385	20.5
Fe_2O_3-500	130.3	19.8	2.02	0.266	9.6
Fe_2O_3-600	107.7	31.2	2.24	0.202	4.7

$$(NH_4)_2CO_3 \longrightarrow 2\,NH_4^+ + CO_3^{2-} \quad \text{(i)}$$
$$FeSO_4 \longrightarrow Fe^{2+} + SO_4^{2-} \quad \text{(ii)}$$
$$Fe^{2+} + CO_3^{2-} \longrightarrow FeCO_3 \quad \text{(iii)}$$
$$2\,Fe^{3+} + C_6H_8O_6 \longrightarrow 2\,Fe^{2+} + C_6H_6O_6 + 2H^+ \quad \text{(iv)}$$
$$2\,CO_3^{2-} + 2\,H_2O \longrightarrow 2HCO_3^- + 2\,OH^- \quad \text{(v)}$$
$$Fe^{2+} + 2\,OH^- \longrightarrow Fe(OH)_2 \quad \text{(vi)}$$
$$Fe(OH)_2 + CO_3^{2-} \longrightarrow FeCO_3 \quad \text{(vii)}$$
$$Fe^{3+} + 3\,OH^- \longrightarrow Fe(OH)_3 \quad \text{(viii)}$$
$$Fe(OH)_2 + 2Fe(OH)_3 \longrightarrow Fe_3O_4 + 4\,H_2O \quad \text{(ix)}$$

Scheme 1. Proposed reaction mechanism for formation of $FeCO_3$ or a mixture of $FeCO_3$ and Fe_3O_4.

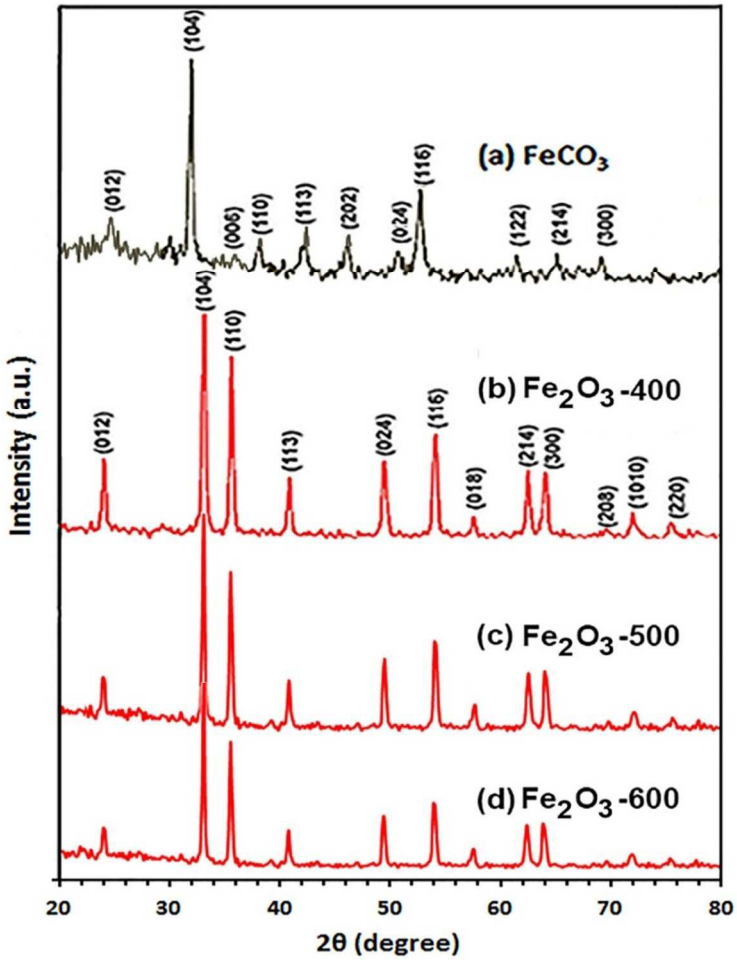

Fig. 1. XRD patterns of the as-synthesized $FeCO_3$ (a), and α-Fe_2O_3 nanoparticles produced at: 400 ºC (b), 500 ºC (c), and 600 ºC (d).

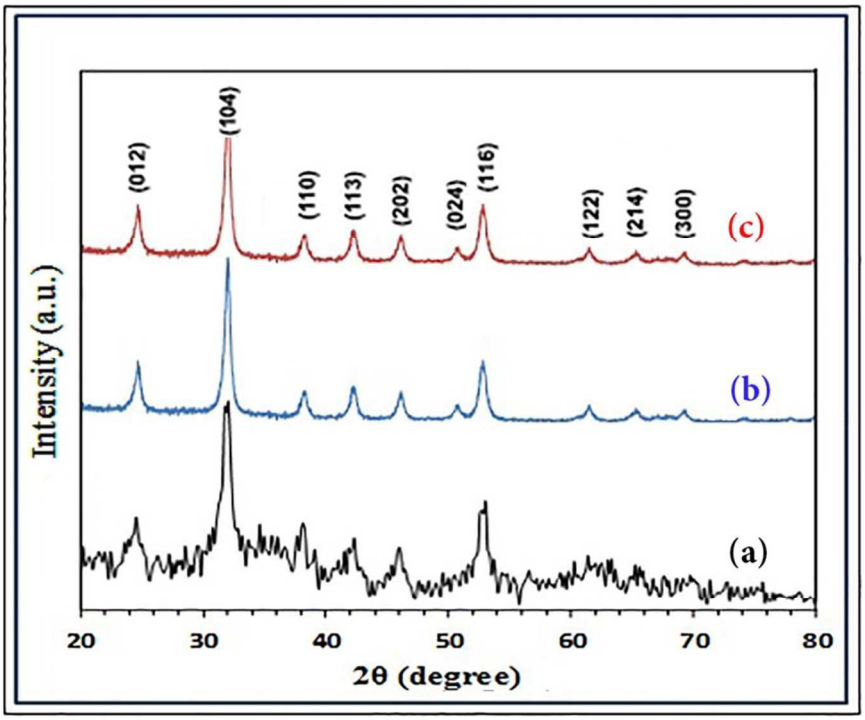

Fig 2I(a-c). XRD patterns of the $FeCO_3$ samples prepared under hydrothermal conditions for 3 h with molar ratio of 1:3:6 for iron sulfate:ascorbic acid:ammo-nium carbonate, respectively, at different temperatures: 120 (a), 140 (b), and 160 ºC (c).

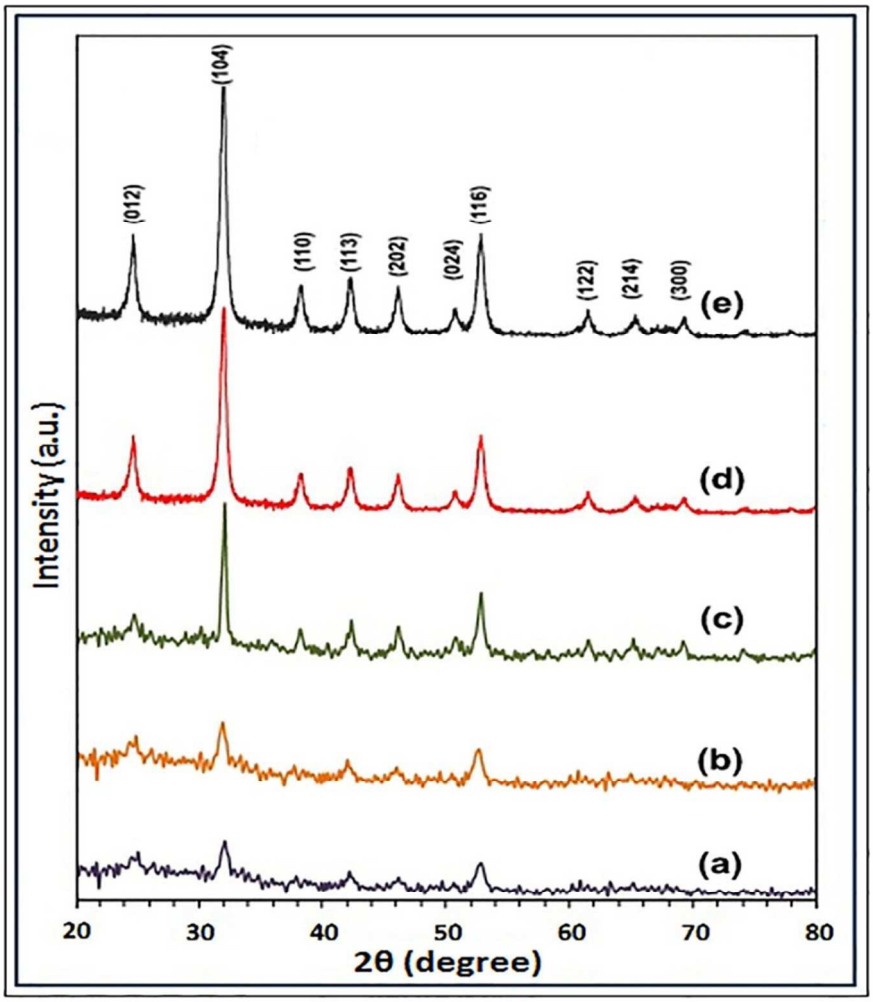

Fig.2II(a-e). XRD patterns of the samples prepared under hydrothermal conditions with molar ratio of 1:3:6 for iron sulfate:ascorbic acid:ammonium carbonate, respectively, at 140 ºC for 0.5 (a), 1 (b), 1.5 (c), 2 (d), and 3h (e).

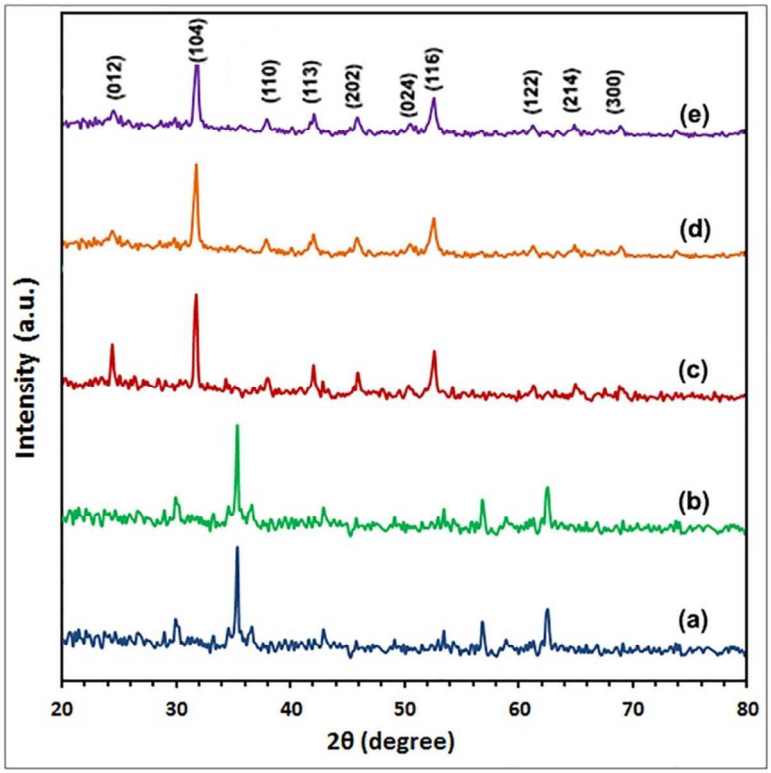

Fig. 2III(a-e). XRD patterns of the samples prepared under hydrothermal conditions with Fe^{2+}:CO_3^{2-} molar ratios of 1:6 (a), and with Fe^{2+}:ascorbic acid:CO_3^{2-} molar ratios of 1:0.5:6 (b), 1:1:6 (c), 1:2:6 (d), and 1:3:6 (e), at 140 ºC for 1.5h.

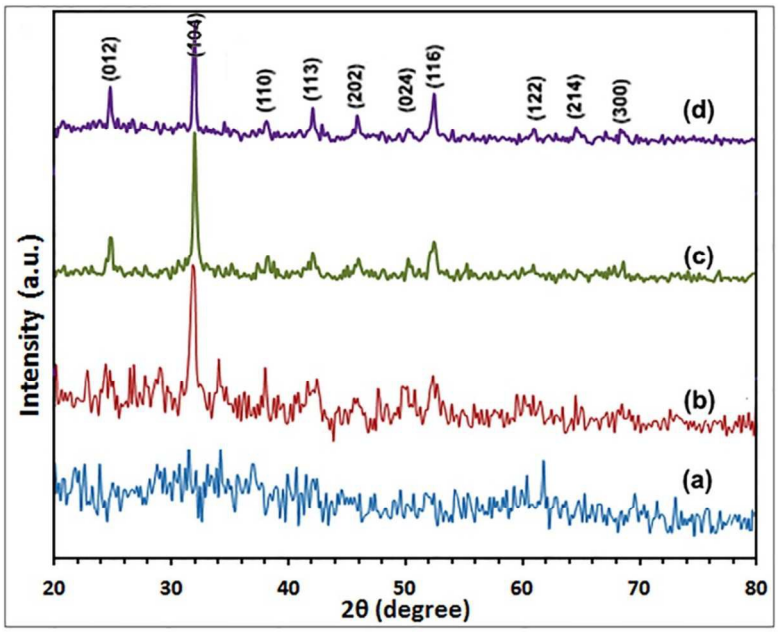

Fig. 2IV(a-d). XRD patterns of the samples prepared under hydrothermal conditions with Fe^{2+}:ascorbic acid:CO_3^{2-} molar ratios of 1:1:**1** (a), 1:1:**2** (b), 1:1:**3** (c), and 1:1:**6** (d), at 140 ºC for 1.5h.

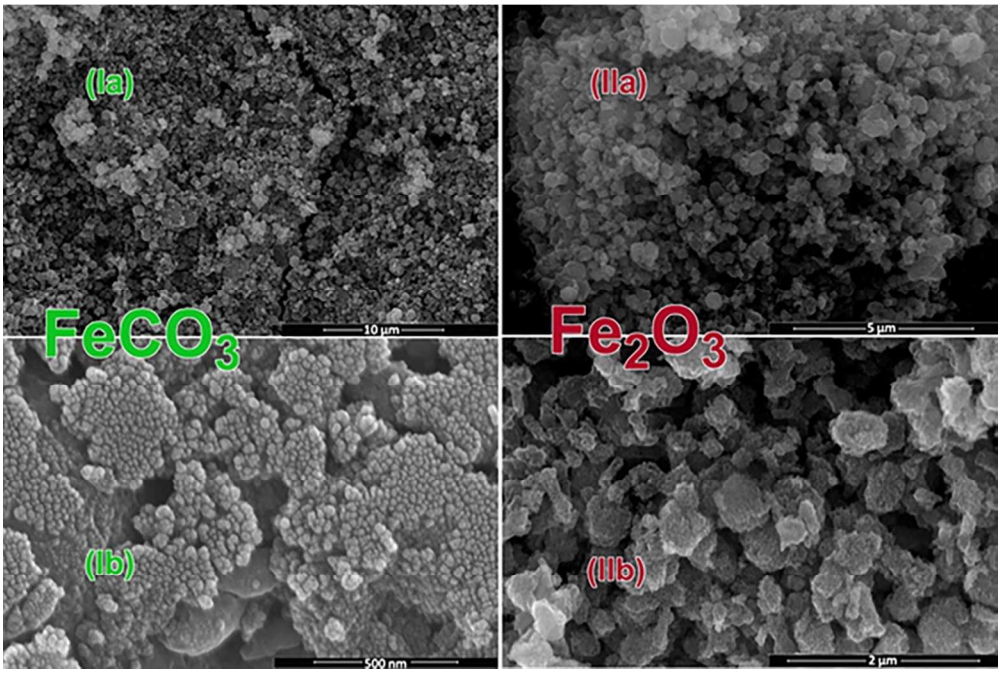

Fig.3. FE-SEM images for as-synthesized $FeCO_3$ (Ia,Ib), and α-Fe_2O_3 produced at 600 ºC (IIa,IIb); low (Ia,IIa) and high (Ib,IIb) magnification images.

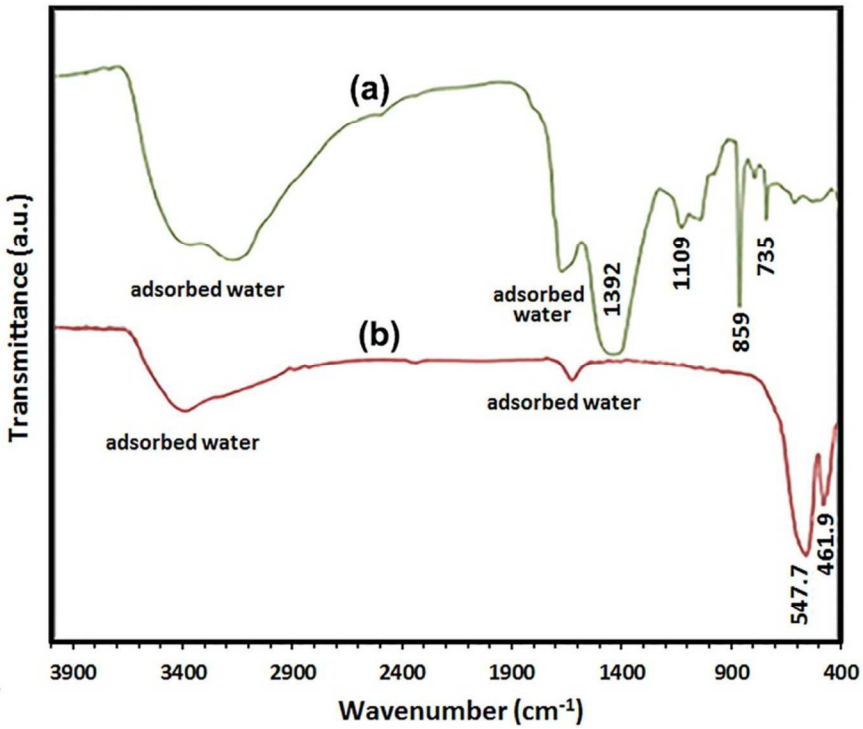

Fig. 4. FT-IR spectra of the as-synthesized $FeCO_3$ (a), and α-Fe_2O_3 produced at 600 ºC (b).

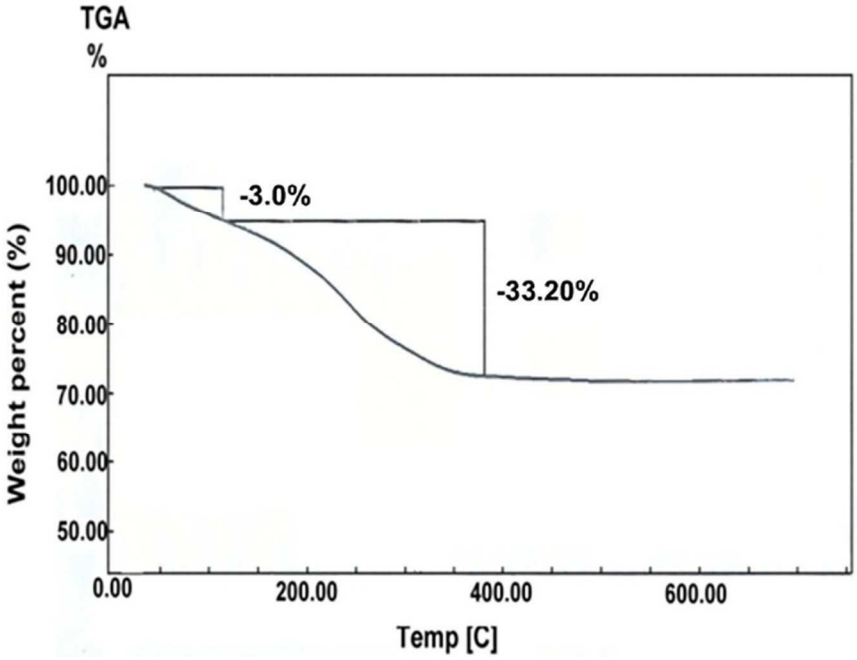

Fig. 5. Thermo-gravimetric analysis of the as-synthesized $FeCO_3$ under N_2 gas.

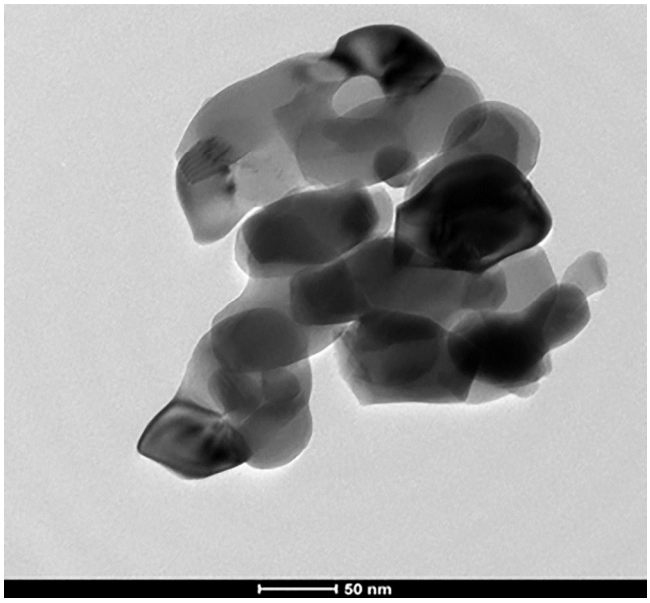

Fig. 6.HR-TEM image of the as-produced α-Fe_2O_3 nanoparticles produced at 600 ºC.

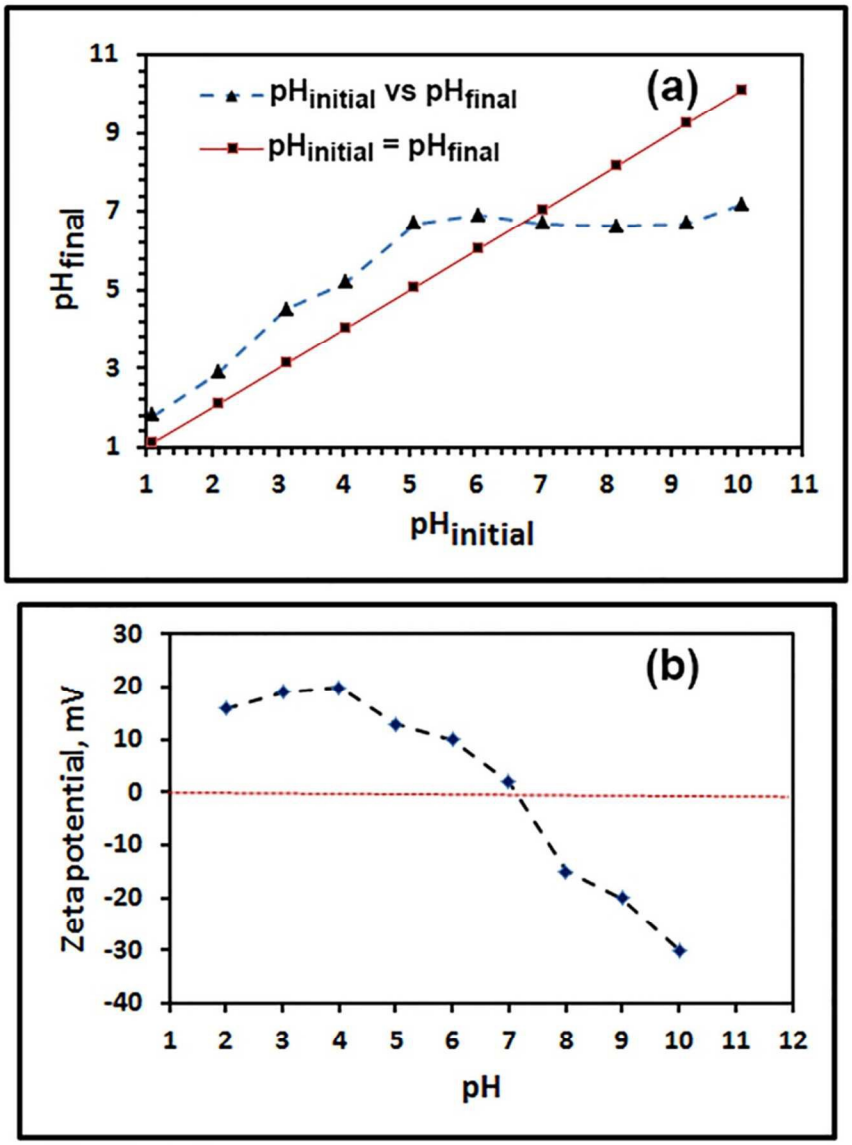

Fig. 7. $pH_{initial}$ against pH_{final} plot for determination of pH_{pzc} for of α-Fe_2O_3 nanoparticles **(a), and** Zeta potential of α-Fe_2O_3 nanoparticles as a function of pH (b).

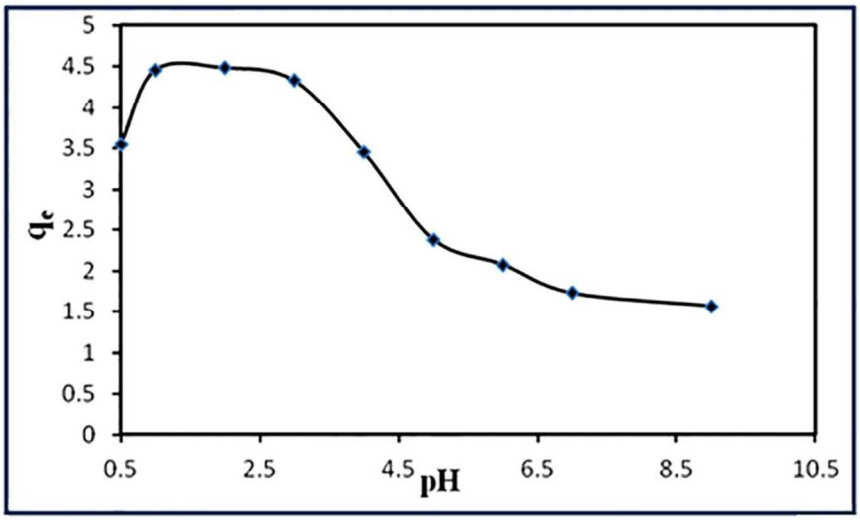

Fig. 8. pH influence on RR dye removal efficiency.

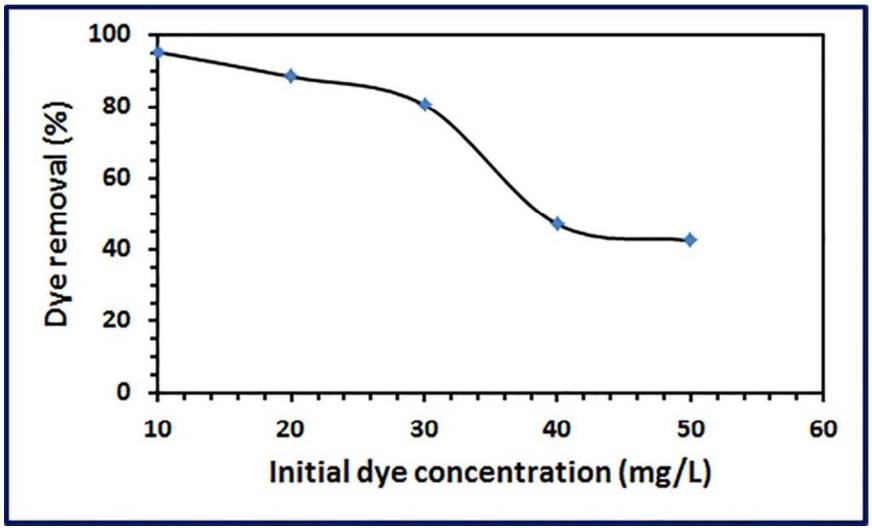

Fig. 9. Influence of initial RR dye concentration on its removal percentage.

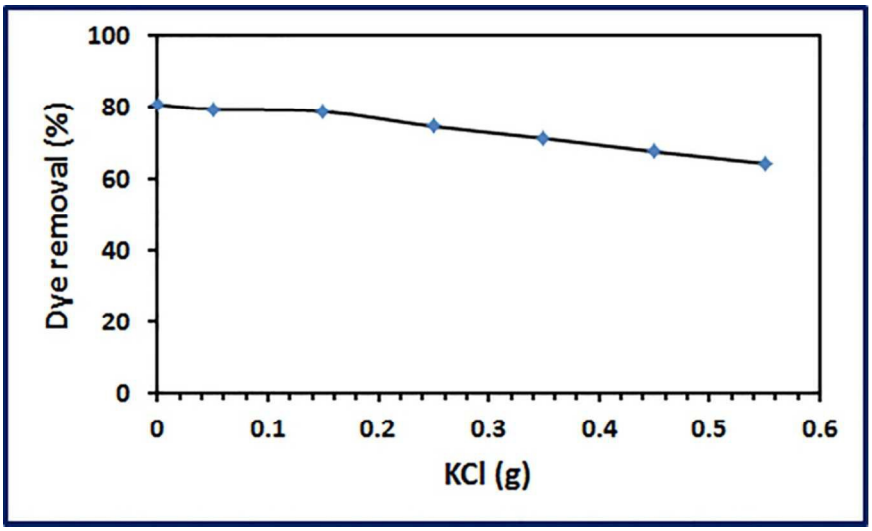

Fig. 10. Effect of KCl concentration on RR dye removal percentage.

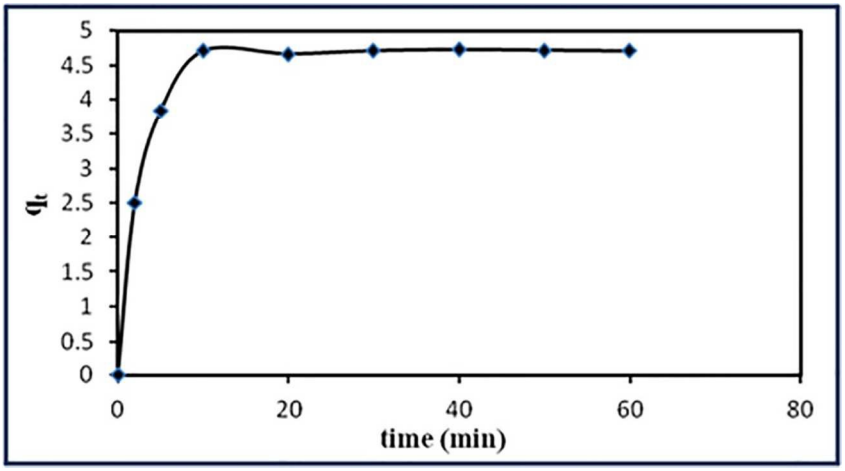

Fig. 11. Influence of contact time on RR dye adsorption by α-Fe_2O_3 nanoparticles.

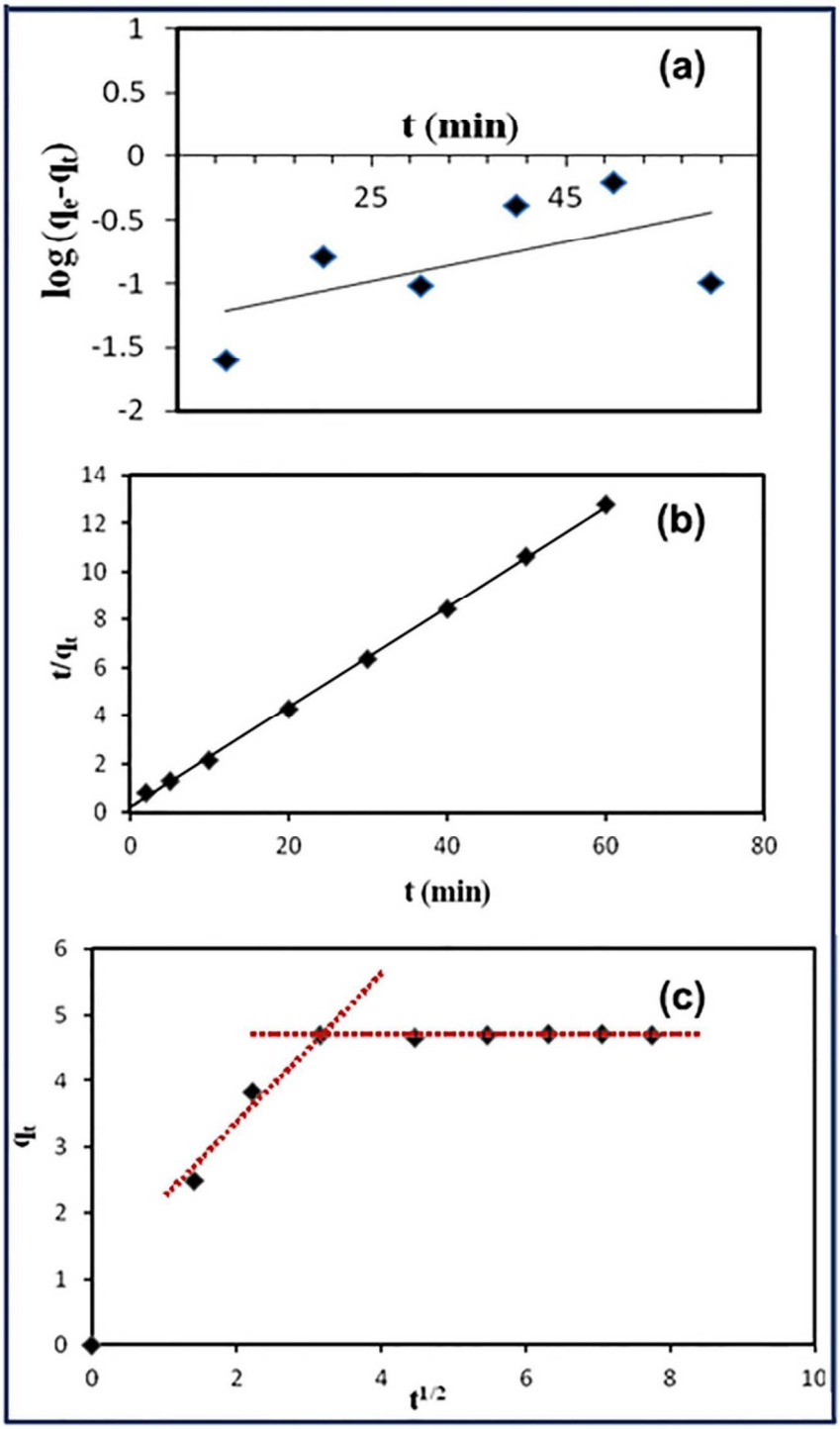

Fig. 12. Adsorption kinetic; (a) pseudo-first-order, (b) pseudo-second-order, and (c) intra-particle diffusion model, for RR dye adsorption onto α-Fe_2O_3 nanoparticles.

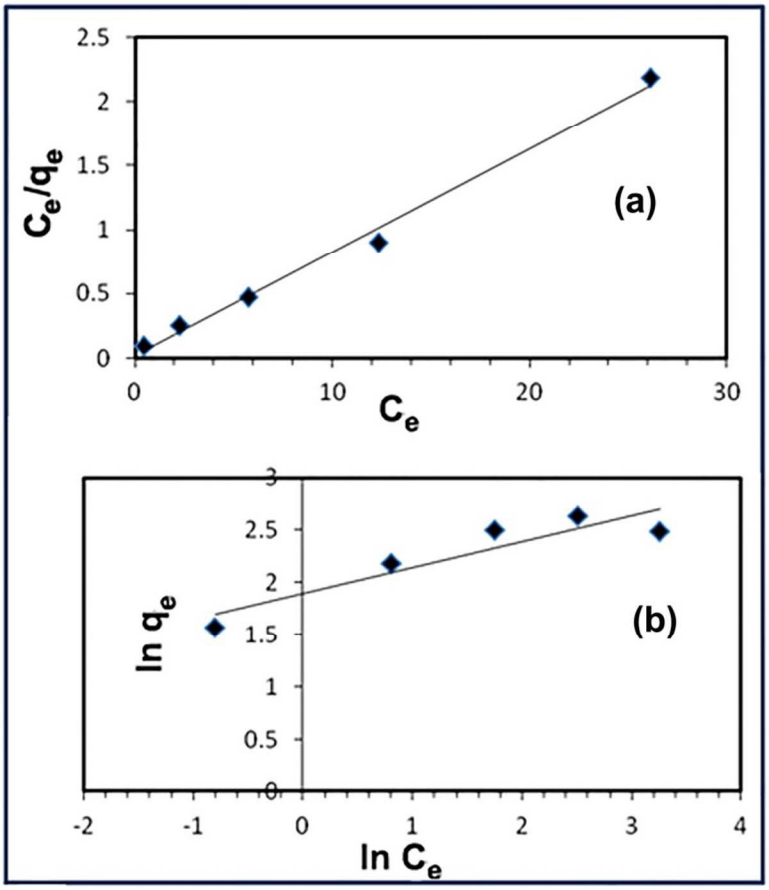

Fig. 13. Langmuir (a) and Freundlich (b) isotherms for RR dye adsorption onto α-Fe_2O_3 nanoparticles.

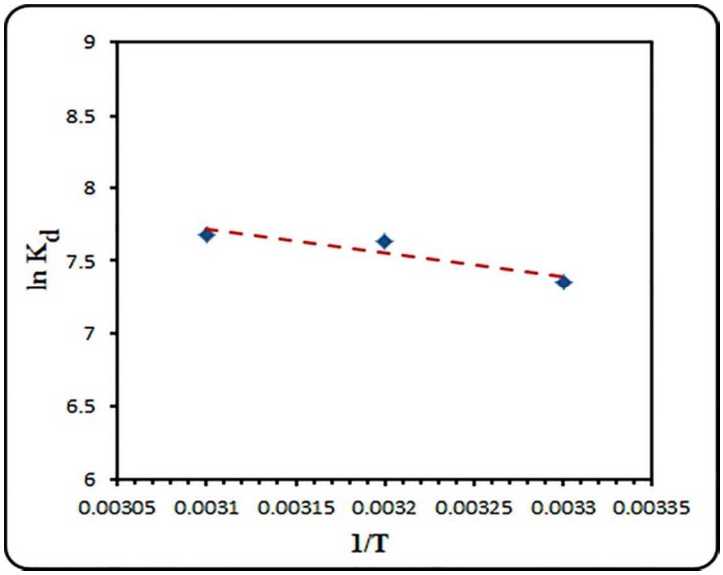

Fig. 14. Plot of ln K_c against 1/T for RR dye adsorption on α-Fe_2O_3 nanoparticles.

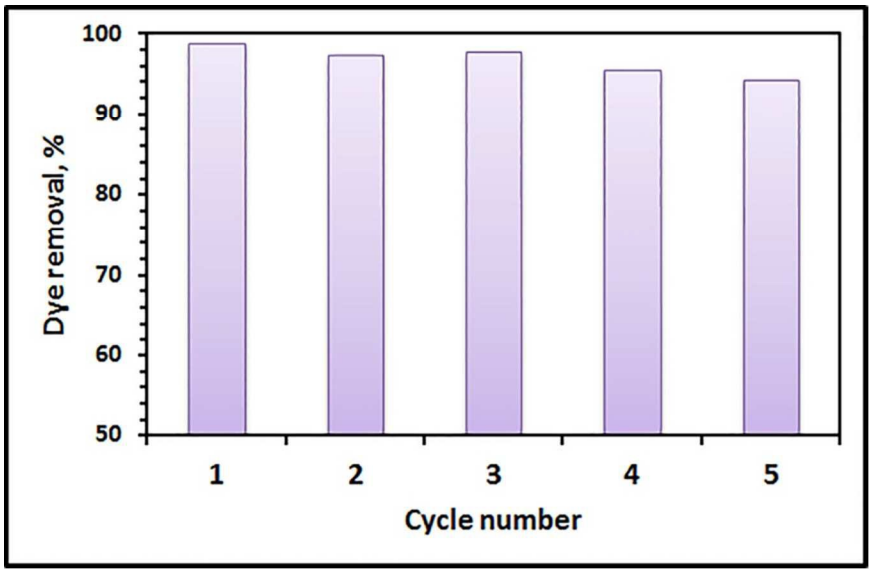

Fig. 15. RR dye removal efficiency of intact and regenerated α-Fe_2O_3 adsorbent during five adsorption/desorption cycles at 298 K.

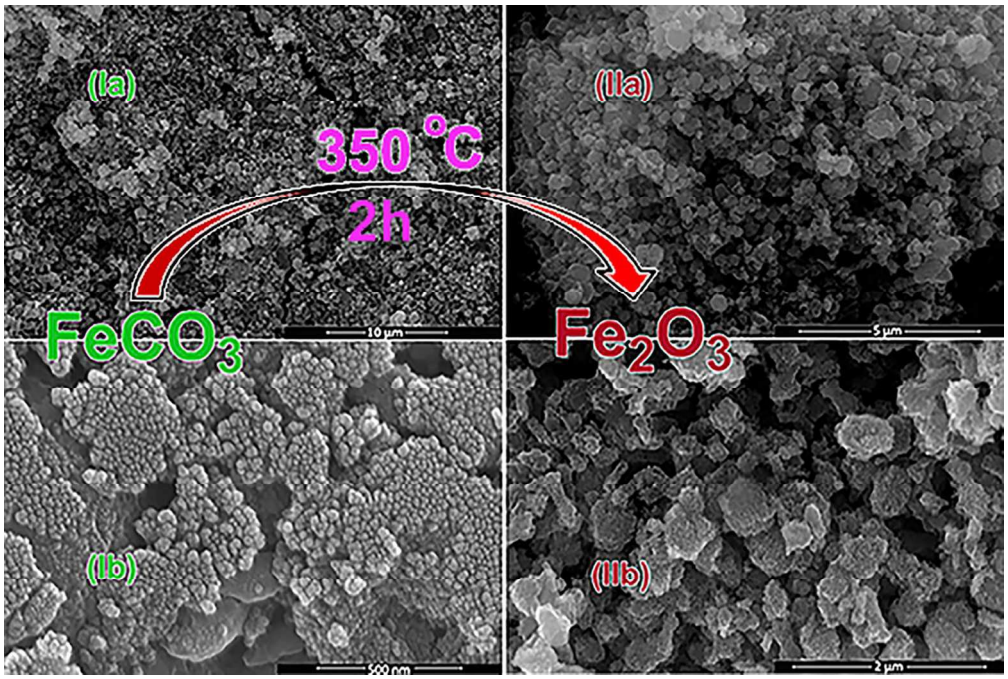

152x101mm (300 x 300 DPI)